International Communications in Heat and Mass Transfer 156 (2024) 107592

Contents lists available at ScienceDirect

International Communications in Heat and Mass Transfer

journal homepage: www.elsevier.com/locate/ichmt

Capillary-enhanced two-phase micro-cooler using copper-inverse-opal wick with silicon microchannel manifold for high-heat-flux cooling application

Heungdong Kwon [a], Qianying Wu [a], Daeyoung Kong [a], Sougata Hazra [a], Kaiying Jiang [a], Sreekant Narumanchi [c], Hyoungsoon Lee [b], James W. Palko [d], Ercan M. Dede [e], Mehdi Asheghi [a], Kenneth E. Goodson [a,f,*]

[a] Department of Mechanical Engineering, Stanford University, Stanford, CA 94305, USA
[b] School of Mechanical Engineering, Chung-Ang University, Seoul 06974, South Korea
[c] National Renewable Energy Laboratory, Golden, CO 80401, USA
[d] Mechanical Engineering, University of California, Merced, CA 95343, USA
[e] Electronics Research Department, Toyota Research Institute of North America, Ann Arbor, MI 48105, USA
[f] Department of Material Science and Engineering, Stanford University, Stanford, CA 94305, USA

ARTICLE INFO

Keywords:
Porous metal surfaces
Thermal management
Energy-efficient cooling
Capillary-enhanced boiling
Silicon microchannel manifold

ABSTRACT

In this work, we demonstrate a two-phase capillary-fed boiling micro-cooler that consists of a ≈ 25-μm-thick copper inverse opal (CIO) porous wicking structure for high-heat-flux boiling and a silicon 3D-manifold for distributed liquid delivery and vapor extraction across a 0.5 cm × 0.5 cm heated area. At low inlet water mass flow rates of 1.5 to 1.9 g(min)$^{-1}$, the micro-cooler displays nearly two-phase boiling with exit vapor quality ≈ 1 and a high critical heat flux (CHF) of 253 to 320 W cm^{-2} with low superheat of ≈ 10 °C resulting in a thermal resistance of boiling ≈ 0.025 cm^2 °C W^{-1} or heat transfer coefficient of 0.4 MW m^{-2} °C^{-1}. For higher flow rates of 5, 10, and 15 g(min)$^{-1}$, the micro-cooler exhibits a hybrid single-phase and two-phase cooling regime where the contribution of the sensible heat (single-phase) cooling is *linearly* added to that of the two-phase cooling. For the highest flow rate of 15 g(min)$^{-1}$, the CHF is increased to ≈ 500 W cm^{-2} resulting in an overall thermal resistance of ≈ 0.18 cm^2 °C W^{-1}. However, the two-phase heat transfer effectiveness, which estimates the utilization level of the inlet mass flow rate for two-phase boiling, is reduced to ≈ 0.11. To achieve the best cooling system performances, the micro-cooler must operate *entirely* within the two-phase boiling regime (exit vapor quality or two-phase heat transfer effectiveness ≈ 1). Ideally, the "coolant" should be delivered near its saturation temperature (≈ 100 °C for water), which provides significant advantages for the energy-efficient operation of data centers and power electronics. We present detailed analysis with Infrared and high speed camera images at various inlet flow rates and heat fluxes to understand complex heat transfer in the micro-cooler. Furthermore, a conjugate thermofluidic simulation model, which incorporates the physics of capillary-fed boiling in a porous copper layer, agrees well with the experimental data.

1. Introduction

The worldwide electricity consumption of microelectronics is rapidly increasing due to the growing demand for data processing [1] and power conversion [2]. The continued miniaturization of electronic components has led to a significant increase in power density, reaching heat fluxes as high as 1000 Wcm^{-2} [3]. Such high-power density results in higher junction temperatures, negatively affecting the performance and reliability [3,4]. To mitigate these thermal challenges, a variety of cooling solutions have been developed to efficiently dissipate heat while maintaining operation temperature within acceptable limits. Tuckerman and Pease [5] pioneered the development of silicon microchannel single-phase liquid cooling by removing ~800 W cm^{-2} over a 1 cm × 1 cm heated area but also reported considerable pressure drop (>100 kPa). The thermal resistance between the junction temperature and inlet coolant for data center and power electronics cooling applications is large, which requires inlet coolants to be in the range of ~10–20 °C. This in turn requires a refrigeration facility to reduce the inlet coolant temperature, resulting in an overall increase in the energy required to

* Corresponding author at: Department of Mechanical Engineering, Stanford University, Stanford, CA 94305, USA.
E-mail address: goodson@stanford.edu (K.E. Goodson).

https://doi.org/10.1016/j.icheatmasstransfer.2024.107592

Available online 14 June 2024

Nomenclature

A	Heated area, cm^2
C_p	Specific heat capacity, J kg^{-1} K^{-1}
d	Thickness, m
h	Height, m
h_{fg}	Latent heat of vaporization, J kg^{-1}
I	Electrical current, A
k	Thermal conductivity, W m^{-1} K^{-1}
l	Length, m
$\dot{m}$	Mass flow rate, $g(min)^{-1}$
$\overline{q''}$	Average heat flux across heated area, W cm^{-2}
$\overline{R''}$	Mean thermal resistance cm^2 °C W^{-1}
$\overline{T}$	Average temperature across the heated area, °C
T	Temperature, °C
V	Voltage, V
w	Width, m
x_e	Exit quality (–)

Greek symbol

α	Heat conduction loss constant, Wcm^{-2} $°C^{-1}$
η	Two-phase heat transfer effectiveness (–)
ρ	Water density, kgm^{-3}
φ	Phase of water

Subscript

0	Inlet water temperature
1-φ	Sensible heat transfer contribution
2-φ	Boiling heat transfer contribution
base,CIO	Temperature at the base of CIO wick
capillary	Capillary length
ch	Channel in silicon microchannel manifold
chf	Critical heat flux
cond	Conduction heat transfer contribution
drain	Properties at drain
gap	Gap size between bottom of manifold channel and top surface of CIO wick
heater	Heater
in	Inlet
max	Maximum value
min	Minimum value
NB	Nucleate boiling
overall	Thermal resistance with respect to inlet temperature of liquid
period	Channel period of silicon microchannel manifold
sat	Saturated condition
Si	Silicon substrate below the base of CIO
total	Total heat flux applied to heater
wall	Channel wall in silicon microchannel manifold

operate the cooling system [6,7]. Therefore, it is more desirable to utilize a two-phase cooling technology that has higher convective hear transfer coefficient and can operate with higher inlet coolant temperatures ~60–70 °C but with smaller flow rates [8]. In the past few decades, different types of two-phase cooling schemes have been explored that include but are not limited to flow boiling in microchannels [9–11], two-phase jet impingement cooling [12,13], evaporative spray cooling [14–16], and manifold microchannel heat sinks [17]. Passive two-phase cooling devices (e.g. heat pipe and vapor chamber) utilize porous sintered copper [18] or nanowires [19] or metal dendrite [20] or wire mesh [21,22] or silicon micro-pin array [23] wicks to passively feed liquid into a heated area. The high thermal conductivity porous structures significantly enhance boiling performances owing to numerous nucleation sites and high capillary force for efficient liquid supply within the wick structure [24–26].

Recent works by Zhang and Palko, et al. [24,27] demonstrated feasibility of ultra-high-heat-flux heat removal exceeding 1000 W cm^{-2} with low superheat ≈ 10 °C from narrow (200 to 1000 μm)-bridge copper inverse opal (CIO) wick heaters. Such outstanding thermal performance is due to the capillary-fed liquid flow from both sides of the microbridge and two-phase boiling within the high-thermal-conductivity-and-permeability CIO wick, leading to the complete liquid and vapor phase separation over the width of the bridge. The optimum width of the bridge is twice the capillary wicking length, which is the characteristic length scale where the maximum critical heat flux (CHF) [27] occurs. It is shown that the CHF depends on the effective liquid-vapor permeability within the wicking structure of CIO and depends on the pore and connecting neck diameters as well as the wettability [27].

A large number of researchers have focused on improving the capillary wicking length to enhance boiling performance over larger areas by using hierarchical wicking structures [22,27] or by changing surface wettability [28,29]. In the present work, the area scaling over a 0.5 cm × 0.5 cm microprocessor footprint is achieved by design and microfabrication of a unique silicon (open) microchannel 3D manifold for efficient liquid delivery and vapor extraction to achieve complete vapor-liquid phase separation or vapor exit quality ≈ 1. The specialized 3D silicon manifold basically replicates the narrow microbridge wick structure to cover the much larger area by drawing liquid from the side reservoir using capillary force in open silicon microchannels.

2. Two-phase micro-cooler design

The proposed micro-cooler consists of a 3D silicon (Si) microchannel manifold, and a silicon chip integrated with CIO wick for efficient capillary-fed two-phase boiling, which are brought in contact by simply placing the 3D-manifold on the CIO wick, as shown in Fig. 1(a) and 1(b). The permanent bonding between the microchannels of the manifold and the silicon chip is not required. Two liquid inlet ports are bonded on the Si microchannel manifold to deliver coolant via plastic tubing, as depicted in Fig. 1(a). The microchannels within the manifold are open at the bottom to uniformly distribute liquid over the large-area CIO wick, where the gap between the silicon microchannels and CIO are bridged (filled) by liquid menisci. The wide openings between adjacent microchannels serve as conduits for vapor escape and as pathways to extract excess subcooled liquid from the CIO. Silicon micropillar arrays are fabricated within the 3D manifold plenums to ensure consistent flow distribution across all microchannels of the manifold [30], as displayed in Fig. 1(b). The cold plate includes ≈ 25-μm-thick CIO wick with 0.5 cm × 0.5 cm footprint area, and the aligned heater of matching dimensions is fabricated on the other side of the silicon chip, as shown in Fig. 1(a) and 1(b). Four electrical contact pads are placed for four-probe electrical measurement to accurately estimate the power dissipation rate occurring over the heater. The complete cooler unit is realized by bonding the perimeter of the 3D manifold to the cold plate, thus enclosing the wick within the microchannel array. A more detailed view of the micro-cooler is shown in Fig. 1(c) and 1(d), highlighting key dimensions of the manifold channels and the paths for coolant and vapor flow. The applied heat flux by the heater initiates boiling within the CIO layer and both the vaporized water and any subcooled liquid can exit through the gap between the microchannels of the manifold.

3. Fabrication

The microfabrication process for the CIO cold plate (Steps i to vi) is presented in Fig. 2(a). First, a ≈ 390-μm-thick silicon wafer is prepared,

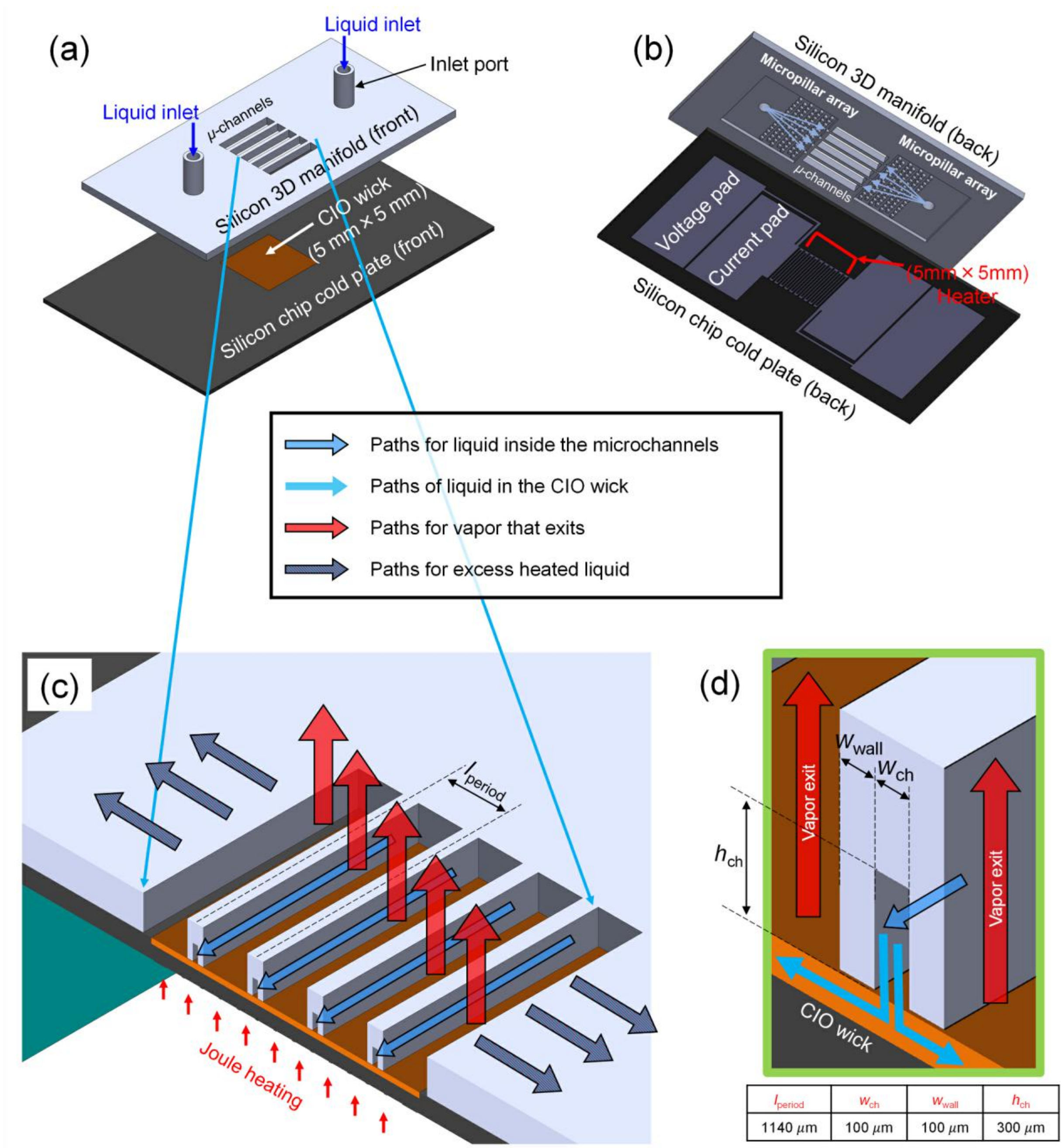

Fig. 1. Illustration of a capillary-assisted micro-cooler that consists of an integrated silicon microchannel manifold and a silicon chip. (a,b) Silicon microchannel manifold and cold plate in two different isometric front and backside views. One side of the silicon chip is coated with CIO microstructures for improved thermal performance, while a heater is micropatterned on the other side. (c) An enlarged view to illustrate flow paths within the micro-cooler. The supplied liquid is delivered along each channel (blue color arrows), and then is uniformly distributed over the CIO wick. Vaporized water exits vertically (red color arrows), while any excess liquid flows sideways and then to the drains (blue/red color arrows). (d) The schematic and accompanying table detail the dimensions of the silicon manifold and the pathways for liquid and vapor. (For interpretation of the references to color in this figure legend, the reader is referred to the web version of this article.)

and a ≈ 270-nm-thick silicon dioxide (SiO_2) layer is grown on both sides of the silicon wafer at 1050 °C in the furnace for 19 min (Step i). The photoresist is spin-coated, and a 0.5 cm × 0.5 cm square area is patterned. The exposed SiO_2 layer is completely etched using a reactive-ion plasma etcher. The remaining photoresist mask is removed by using acetone. A second layer of photoresist is spin-coated on the same side of the wafer and the micro-pin array is patterned over the same 0.5 cm × 0.5 cm area with accurate alignment. The exposed silicon surface through the photoresist is etched to a depth of approximately 3 μm using deep reactive-ion etching (DRIE) process, creating the thin Si micro-pin array (Step ii). This micro-pin array provides support for a sacrificial latex bead template, preventing its delamination from the silicon surface during copper electroplating for the CIO layer. The photoresist residues are completely removed by immersing the wafer in Piranha solution for 20 min at 120 °C. We perform the additional 25-μm etching of the exposed silicon surface to ensure the top surface of the CIO layer aligns with the silicon wafer surface (Step iii). For the opposite side of the wafer, we pattern the aligned heater using the conventional lift-off process (Step iv) with ≈ 100-nm-thick platinum and ≈ 10-nm-thick titanium adhesion layers deposited by using an electron beam evaporator. The integrated heater applies heat flux to the wick area at the other side. An ≈ 100-nm gold layer atop a 10-nm titanium adhesion layer is

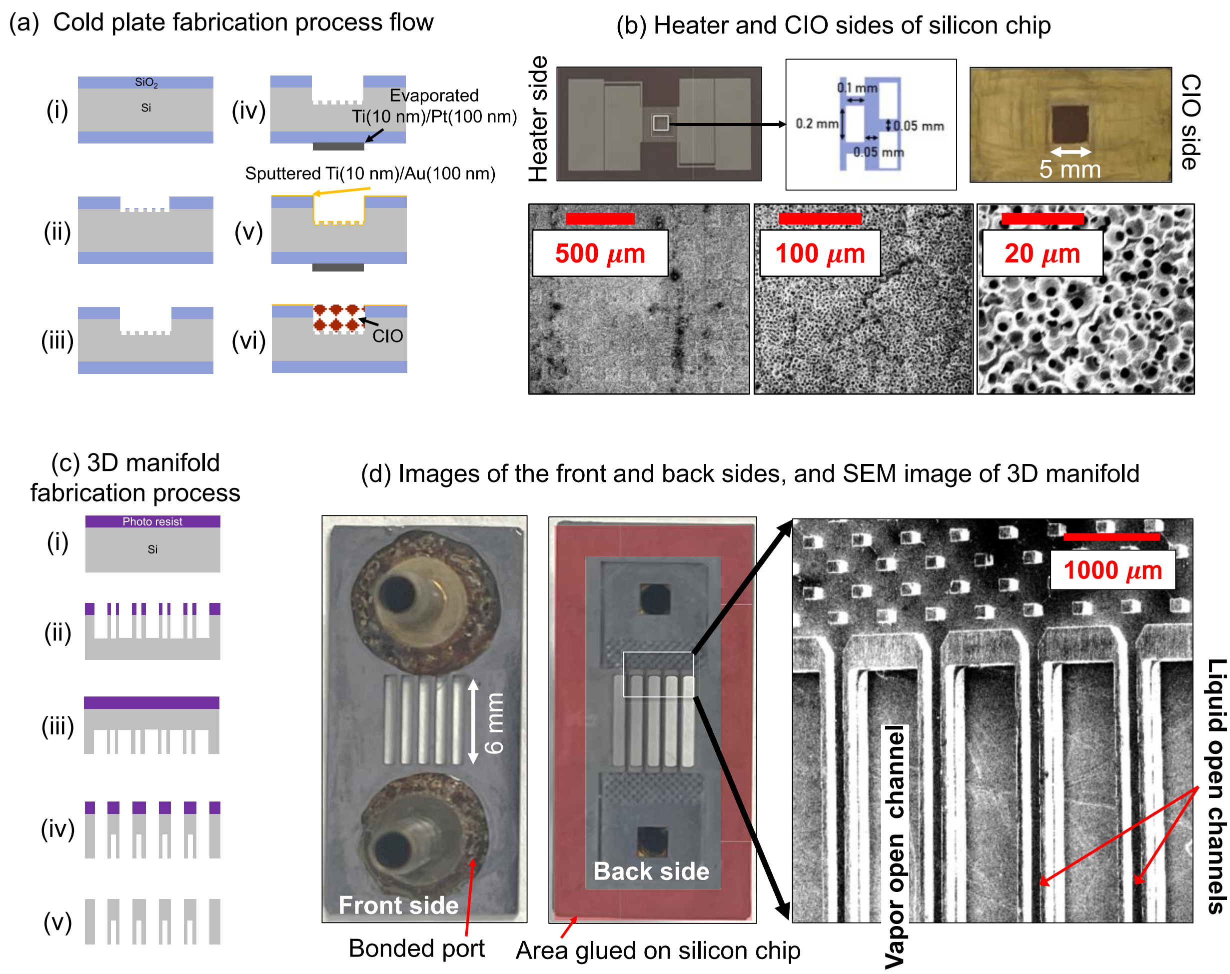

Fig. 2. Fabrication details and final devices of the silicon chip cold plate and silicon 3D manifold. (a) Fabrication process of the cold plate. (b) Optical images of the back and front sides of the cold plate, showing mesh heater dimensions and SEM images of the CIO. (c) Fabrication process of the 3D manifold. (d) Optical images of the front and back sides of the manifold. The SEM image of the manifold's backside reveals the pillar array, open liquid delivery, and vapor exit microchannels. Note that the 3D manifold is glued (red shade) to the periphery of the cold plate, while the open channels are simply pressed against the CIO cold plate, where a liquid meniscus is bridged between the microchannel and the CIO cold plate. (For interpretation of the references to color in this figure legend, the reader is referred to the web version of this article.)

sputtered on the thin silicon pin array to create a conformal electrode layer (Step v), on which the CIO layer is electroplated. Both sides of the fabricated cold plate are shown in Fig. 2(b). A mesh-type heater design allows for uniform heat flux distribution over the active area compared to the serpentine configuration [31] and the resulting electrical resistance of the heater is measured to be ≈ 20 Ω. For the wick side of the cold plate, we performed electroplating to create ≈ 25-μm-thick CIO layer. We use a commercial sulfate latex bead solution with a mean sphere diameter ≈ 5.2 μm for a sacrificial template for electroplating porous copper. This bead solution is applied over thin pillar array structures coated with a sputtered gold layer and is left to completely evaporate. Once the solution evaporates, the beads form a settled layer, which is sintered at 107 °C for an hour in the oven. The sintered bead layer acts as the sacrificial layer for the electroplating of copper. During the electroplating process, the electrical current density is maintained at ≈ 20 mA(cm)$^{-2}$. Following the electroplating, the sacrificial latex layer is dissolved in tetrahydrofuran solvent for an hour, resulting in a permeable porous copper layer. As shown in Fig. 2(b), the scanning electron microscopy (SEM) images of the porous copper are clearly visible, and the pore-to-neck diameter ratio is characterized as ≈ 0.5.

The fabrication process of a 3D silicon microchannel manifold (Step i to v) is displayed in Fig. 2(c). a ≈ 650-μm-thick silicon wafer is used for the substrate. We pattern the microchannels using photolithography and etch them to a depth of ≈ 300 μm using DRIE (Step i and ii). Any residual photoresist is completely removed by immersing the wafer in Piranha solution. For the rear side, the aligned microchannels and apertures with the microchannels on the front side are patterned with photolithography, followed by DRIE. The etching continues until the etchings on the front side are accessible from the backside of the wafer (Step iii and iv). Finally, any remaining photoresist is thoroughly removed by soaking the sample in Piranha solution for 20 min at 120 °C (Step v). The tubing inserts are carefully bonded to the two holes located at the sides of the manifold using EPO-TEK 353ND epoxy. The optical images of both sides of the fabricated manifold, and the SEM image of the backside are shown in Fig. 2(d). The SEM image reveals the micropillar array in the plenum area, the open microchannels, and the phase separation apertures. The prepared 3D manifold and cold plate are bonded at the perimeter of the manifold using a cyanoacrylate-based adhesive.

4. Experiment setup

To facilitate the thermofluidic experiment, as shown in Fig. 3(a), a 3D-printed resin polymer sample holder is fabricated to accommodate the micro-cooler chip while providing the necessary support for the chip, the fluidic delivery, the drainage lines, as well as the electrical and optical access from the backside of the cold plate. The manifold and cold plate combination is carefully secured on the sample holder using silicone grease to prevent coolant leakage. The proposed capillary-fed

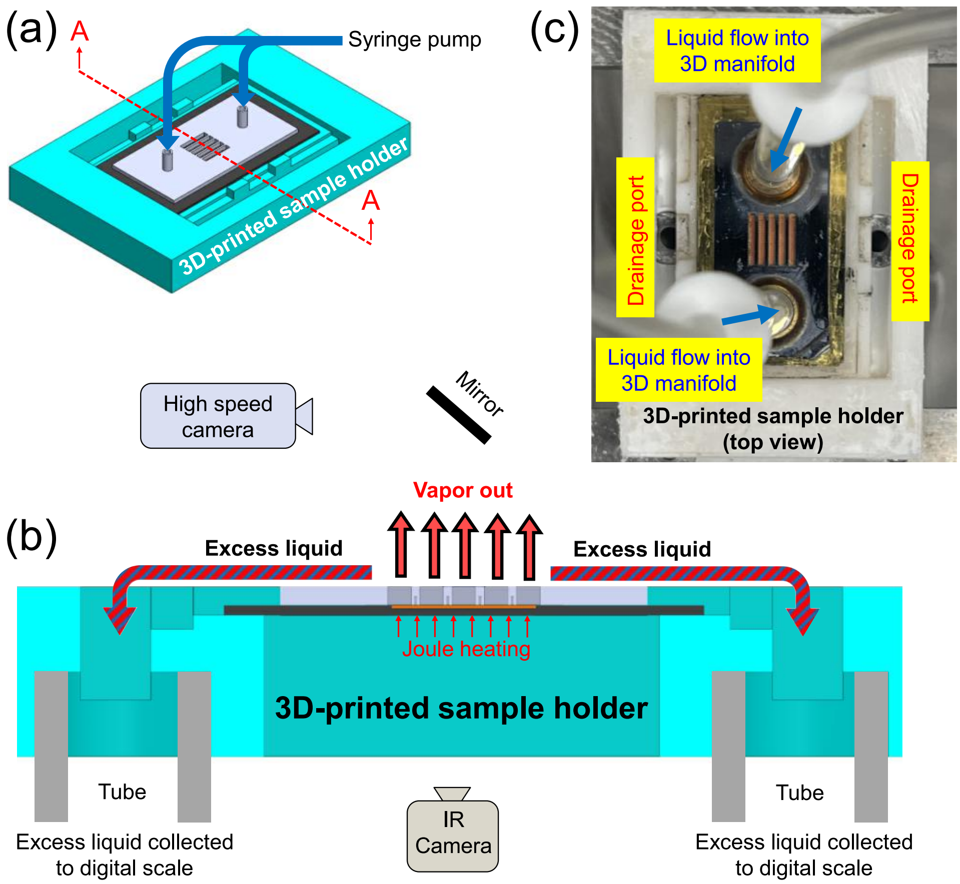

Fig. 3. Experiment details. (a) Illustration of the micro-cooler with a 3D-printed sample holder used in the experiment. (b) Cross-sectional image (A-A) showing the experimental apparatus, highlighting the pathways for liquid delivery and vapor extraction, as well as the excess liquid bypass to the drainage slots. (c) Optical image of the micro-cooler placed on the sample holder.

micro-cooler does not require a pump for flow delivery in two-phase heat transfer operation (exit vapor quality $\approx$ 1). However, to thoroughly examine both the single-phase and two-phase heat transfer regimes, we use a syringe pump to finely control the liquid supply into both inlet ports of the 3D microchannel manifold. The cross-sectional view (A-A) of the micro-cooler integrated with the sample holder, along with a detailed experimental setup, is illustrated in Fig. 3(b). An electrical current along the mesh heater at the base of the cold plate is applied using a power supply and the voltage drop is measured with a multimeter. An electrical current is measured from the voltage drop across a 0.1 Ω shunt resistor, which is connected to the heater in series. The total power generation of the heater is deduced by the multiplication of the measured voltage drop across the mesh heater and the measured electrical current. By tracking the temporal fluctuation of the electrical resistance, when the electrical resistance surge occurs near the dry-out, the power supply is promptly deactivated to prevent any thermal-induced damage on the micro-cooler. A critical heat flux is identified by a rapid increase in the electrical resistance of the heater. If the CHF is not observed, we elevate the voltage of the power supply. During each iteration, the system is closely monitored for any rapid surge in the electrical resistance that would imply the onset of CHF. Along with the electrical measurements, the temperature map of the 0.5 cm × 0.5 cm heater is recorded with the infrared (IR) camera (Teledyne FLIR, A600), which is situated below the sample. To minimize the emissivity variation, black paint is sprayed over the heater, setting the emissivity value at 0.95. We calibrate the measured temperature using the IR camera with the temperature reading from the thermocouple, which shows an error in temperature measurement that falls within 2 °C for the wide temperature range spanning from ambient temperature to 200 °C. It is noted that the sensitivity of the IR measurement is better than 0.1 °C, and hence we can monitor the shift in superheat for different mass flow rates. Additionally, to closely monitor the boiling dynamics over the CIO wick, a high-speed camera is used (IX Cameras, i-SPEED 7 series). Multiple mirrors direct the field view of the wick toward the camera. For higher flowrates, we provide an oversupply of water. A portion of the water changes its phase from liquid to vapor, while the remaining excess water flows over the 3D microchannel manifold toward both sides, as seen in Fig. 3(b). This excess water is collected through the drain pans and holes integrated in the 3D-printed sample holder, as shown in Fig. 3(c). The amount of liquid passing through the drain is accurately measured using a digital scale. The total amount of fluid discharged over a set duration is calculated to derive the mass flow rate of drained water. The container for the drained water is connected to a gentle vacuum system to efficiently extract the unevaporated water.

5. Data reduction and uncertainty

The total power is determined by the product of the applied electrical current (I) and the voltage drop across the heater (V_{heater}). To obtain the total heat flux, this total power is normalized by the area of the heater (A):

$$\overline{q''}_{total} = \frac{IV_{heater}}{A} \tag{1}$$

The average temperature of the CIO base is estimated by accounting for the temperature drop across the thickness of the silicon substrate (d_{Si}) between the heater and the base of CIO wick. This is calculated by subtracting the temperature drop from the measured average temperature of the heater using IR camera over 0.5 cm × 0.5 cm area as the following equation:

$$\overline{T}_{\text{base,CIO}} = \overline{T}_{\text{heater}} - \frac{d_{\text{Si}}}{k_{\text{Si}}}\overline{q''}_{\text{total}} \tag{2}$$

The mass flow rate that undergoes boiling (two-phase heat transfer) is determined by subtracting the flow rate measured at the drain ($\dot{m}_{\text{drain}}$) from the inlet mass flow rate ($\dot{m}_{\text{in}}$):

$$\dot{m}_{2-\varphi} = \dot{m}_{\text{in}} - \dot{m}_{\text{drain}} \tag{3}$$

To estimate the individual heat flux contributions in the cooler, the total heat flux is divided into three distinct heat flux contributions: sensible or single-phase heat transfer to the water, phase change or two-phase heat transfer, and heat conduction loss through the cooler, respectively:

$$\overline{q''}_{\text{total}} = \overline{q''}_{1-\varphi} + \overline{q''}_{2-\varphi} + \overline{q''}_{\text{cond}} \tag{4}$$

In addition, the heat flux due to single-phase heat transfer ($\overline{q''}_{1-\varphi}$) can be divided into two components. The one ($\overline{q''}_{1-\varphi,T_{\text{sat}}}$) represents the heat flux required to raise the temperature of the mass flow rate that undergoes the phase change from T_{in} to T_{sat}:

$$\overline{q''}_{1-\varphi,T_{\text{sat}}} = \frac{\dot{m}_{2-\varphi}C_{\text{p}}(T_{\text{sat}} - T_{\text{in}})}{A} \tag{5}$$

The other ($\overline{q''}_{1-\varphi,T_{\text{drain}}}$) represents the heat flux required to raise the temperature of the mass flow to the drain ($\dot{m}_{\text{drain}}$) from T_{in} to T_{drain}:

$$\overline{q''}_{1-\varphi,T_{\text{drain}}} = \frac{\dot{m}_{\text{drain}}C_{\text{p}}(T_{\text{drain}} - T_{\text{in}})}{A} \tag{6}$$

Hence, the heat flux due to single-phase heat transfer can be represented by summing these two components:

$$\overline{q''}_{1-\varphi} = \overline{q''}_{1-\varphi,T_{\text{sat}}} + \overline{q''}_{1-\varphi,T_{\text{drain}}} = \frac{\dot{m}_{2-\varphi}C_{\text{p}}(T_{\text{sat}} - T_{\text{in}})}{A} + \frac{\dot{m}_{\text{drain}}C_{\text{p}}(T_{\text{drain}} - T_{\text{in}})}{A} \tag{7}$$

To estimate single-phase heat transfer rate in the micro-cooler system, it is essential to determine the temperature at the drain. However, the cooler is operated at a relatively low inlet flow rate, well below 20 g (min)$^{-1}$, resulting in a highly intermittent flow at the drain, which renders the measurement of T_{drain} inaccurate. In cases where the flow rate at the drain is negligible, implying that all supplied liquid is utilized in the boiling process, the heat flux due to single-phase heat transfer can be simplified as follows:

$$\overline{q''}_{1-\varphi,\dot{m}_{\text{drain}}=0} = \frac{\dot{m}_{2-\varphi}C_{\text{p}}(T_{\text{sat}} - T_{\text{in}})}{A} \tag{8}$$

However, if the mass flow rate at the drain is non-zero, the contribution of single-phase heat transfer can be inferred by a linear fit to the experimental data between the total heater heat flux ($\overline{q''}_{\text{total}}$) and $\overline{T}_{\text{base,CIO}}$, for temperatures below T_{sat}. Once the water reaches its saturation temperature, the two-phase heat transfer is primarily driven by boiling, [21,24,32,33], and thus the heat flux associated with boiling can be calculated using the latent heat of vaporization.

$$\overline{q''}_{2-\varphi} = \frac{h_{\text{fg},T_{\text{sat}}}\dot{m}_{2-\varphi}}{A} \tag{9}$$

There is also heat conduction loss through the silicon substrate. To quantify the "upper limit" of this heat conduction loss, we measure the mean temperature increase of the heater against the applied heat flux. This measurement is conducted on the dry sample to ensure that the temperature rise is exclusively due to the heat conduction through the silicon substrate. The applied heat flux is found to be linearly proportional to the mean temperature rise of the heater from room temperature (T_0) with a proportionality constant, $\alpha = 0.1446$ W cm^{-2} °C^{-1}:

$$\overline{q''}_{\text{cond}} = \alpha(\overline{T}_{\text{heater}} - T_0) \tag{10}$$

The mean thermal resistance over the heated area for the two-phase heat transfer during boiling can be represented as the following equation:

$$\overline{R''}_{2-\varphi} = \frac{\overline{T}_{\text{base,CIO}} - T_{\text{sat}}}{\overline{q''}_{2-\varphi}} \tag{11}$$

To evaluate the overall thermal performance, we define the thermal resistance of the micro-cooler with respect to the inlet liquid temperature.

$$\overline{R''}_{\text{overall}} = \frac{\overline{T}_{\text{heater}} - T_{\text{in}}}{\overline{q''}_{\text{total}}} \tag{12}$$

For mass flow rates >1.9 g(min)$^{-1}$, excess liquid that does not undergo a phase change process sloshes around the micro-cooler. In this scenario, a combination of capillary wicking and boiling within the CIO and single-phase forced flow over the CIO (in between manifold channels) prevails. To assess how efficiently the cooler utilizes the inlet mass flow rate for boiling, we introduce a metric called the two-phase heat transfer effectiveness (η):

$$\eta = \frac{\dot{m}_{2-\varphi}h_{\text{fg}}}{\dot{m}_{\text{in}}h_{\text{fg}}} = \frac{A\overline{q''}_{2-\varphi}}{\dot{m}_{\text{in}}h_{\text{fg}}} = \frac{A(\overline{q''}_{\text{total}} - \overline{q''}_{\text{cond}} - \overline{q''}_{1-\varphi})}{\dot{m}_{\text{in}}h_{\text{fg}}} \tag{13}$$

It is important to note that in cases where there is no flow rate at the drain, the two-phase heat transfer effectiveness becomes equivalent to the vapor exit quality as ≈ 1, $\eta_{\dot{m}_{\text{drain}}=0} = x_{\text{e},\dot{m}_{\text{drain}}=0} \approx 1$, because all supplied heat is utilized to raise the temperature of the liquid flow from room temperature to the saturation temperature, and nearly all the saturated liquid is turned to vapor. This indicates that in the absence of drain flow, the micro-cooler achieves maximum effectiveness in two-phase heat transfer with an exit vapor quality ≈ 1. In Supplementary Information, the detailed derivations of the two-phase heat transfer effectiveness and the exit vapor quality are provided. The measurement uncertainties are detailed in Table 1. We calculated the propagated errors for the derived parameters based on these measurement uncertainties as outlined in [34]. Table 2 presents the calculated error ranges for the derived parameters along with their sources to the corresponding errors.

6. Results and discussion

Fig. 4(a) presents the measured total heat flux ($\overline{q''}_{\text{total}}$) as a function of the average temperature of CIO wick base ($\overline{T}_{\text{base,CIO}}$) at mass flow rates of 1.5, 1.7, and 1.9 g(min)$^{-1}$. $\overline{T}_{\text{base,CIO}}$ is extracted from the measured average temperature of the heater according to Eq. (2). We recall that the power supply is turned off to protect the sample whenever a sudden temperature rise is observed due to the appearance of local hot spots. Therefore, we denote the heat flux just prior to the complete dry-out of the cooler as the heat flux of nucleate boiling ($\overline{q''}_{\text{total,NB}}$), where no hot spots are observed. Increasing the heat flux by 10 to 20 W cm^{-2} above $\overline{q''}_{\text{total,NB}}$ leads to the formation of hot spots that eventually grow in size across the entire cooler area, resulting in dry-out. Therefore, the critical

Table 1
Uncertainties associated with measurement instruments.

Measurement	Instrument	Uncertainty
Heater voltage	Digital multimeter	±0.0015 %
Heater current	Shunt resistor and digital multimeter	±0.1 %
Liquid inlet temperature	K-type thermocouple	±1 °C
Heater temperature	IR camera	±2 °C
Inlet flow rate	Syringe diameter and syringe pump	±2 %
Mass of collected liquid at drain	Digital scale	±0.1 g
Silicon substrate thickness	Caliper	±15 μm

Table 2
Summary of uncertainty ranges of the derived parameters and the corresponding sources of uncertainties.

Derived parameter	Source of uncertainty	Maximum uncertainty
$\dot{m}_{in}$	Syringe diameter, Syringe pump	2 %
$\dot{m}_{drain}$	Digital Scale	5 %
$\dot{m}_{2-\varphi}$	$\dot{m}_{in}$, $\dot{m}_{drain}$	16 %
$\overline{q}''_{2-\varphi}$	$\dot{m}_{2-\varphi}$	16 %
$\overline{q}''_{total}$	Shunt resistor and digital multimeter	0.1 %
η	$\overline{q}''_{total}$, $\overline{q}''_{2-\varphi}$	15 %
x_e	$\overline{q}''_{total}$, $\overline{q}''_{2-\varphi}$	42 %
$\overline{T}_{heater}$	IR camera	2 °C
$\overline{T}_{base,CIO}$	$\overline{T}_{heater}$, $\overline{q}''_{total}$, d_{Si}, k_{Si} (± 5%)	2 °C
$\overline{R}''_{2-\varphi}$	$\overline{T}_{base,CIO}$, $\overline{q}''_{2-\varphi}$	34 %
$\overline{R}''_{overall}$	$\overline{T}_{heater}$, T_0, $\overline{q}''_{total}$	4 %

heat flux ($\overline{q}''_{CHF}$) where the complete dry-out occurs is comparable to $\overline{q}''_{total,NB}$ within a 10% difference. The experimental boiling data of $\overline{q}''_{total}$ clearly shows a non-linear relationship with $\overline{T}_{base,CIO}$ owing to the onset of boiling (ONB) near the water saturation temperature. A range of (small) flow rates is selected to ensure the flow rate at the drainages is near zero. This is to investigate the characteristics of the capillary-fed two-phase micro-cooler at two-phase heat transfer effectiveness and exit vapor quality ≈ 1. The schematic in Fig. 4(b) depicts the condition where sufficient fluid is supplied to exactly balance the two-phase heat transfer within the CIO wick, and there is no excess fluid to flood or cover the CIO wick, resulting in very small superheat and extraordinarily low mean two-phase thermal resistance ($\overline{R}''_{2-\varphi} \approx 0.02$ cm^2 °C W^{-1} or heat transfer coefficient ≈ 0.5 MW m^{-2} °C^{-1}), as observed in previous studies of capillary-fed heat transfer using a similar CIO to the one used in this study [24,27,35]. Increasing the flow rate from 1.5 to 1.7 g(min)$^{-1}$ raises $\overline{q}''_{total,NB}$ by ≈ 30 Wcm^{-2}, but the electronic scale at the drainage shows no increase in mass at $\overline{q}''_{total,NB}$. This observation suggests that the sensible heat transfer is solely attributed to the increase in water temperature from room temperature to the saturation temperature. The measured increase in heat flux is comparable to the calculated value ≈ 35.6 W cm^{-2}, which represents the combined sensible and boiling heat transfer at a liquid flow rate ≈ 0.2 g(min)$^{-1}$. Increasing the inlet flow rate to 1.9 g(min)$^{-1}$ results in a small flow rate at the drain ≈ 0.12 g(min)$^{-1}$. This implies that the optimum inlet flow rate to achieve an exit vapor quality ≈ 1 is between 1.7 and 1.9 g (min)$^{-1}$.

To investigate the impact of excess liquid supply on the thermal performance of the micro-cooler, the inlet flow rate (≈ 21 °C) is increased to 5, 10, and 15 g(min)$^{-1}$, as depicted in Fig. 5(a). The comparison of boiling curves reveals that increasing the inlet flow rate from 1.9 g(min)$^{-1}$ to 15 g(min)$^{-1}$ leads to a significant enhancement in $\overline{q}''_{total,NB}$ up to ≈ 500 W cm^{-2}. The additional 250 W cm^{-2} is mainly due to the sensible heat contribution from the excess liquid supplied. At high flow rates of 10 and 15 g(min)$^{-1}$, despite the abundance of excess liquid leading to overflow, there is no notable increase in superheat. This observation differs from results seen in previous studies on pool boiling on the similar CIO layer [31], where superheat typically increases monotonically as the input heat flux increases, due to the formation of large bubbles. We postulate that a shallow liquid pool, as illustrated in Fig. 5(b), does not significantly affect superheat, as opposed to a thicker pool. Furthermore, the flow leaking from the gap between the CIO and the microchannel helps to sweep away bubbles emerging from the wick, facilitating efficient bubble removal. This contrasts with the growth of large bubbles in pool boiling conditions, where bubbles can grow to sizes comparable to the heating element.

To obtain further insights into the contribution of the single-phase and two-phase heat transfer, we subtract the estimated total heat loss due to single-phase and heat conduction loss, which correspond to black dashed lines in Fig. 5(a). As depicted in Fig. 5(c), the two-phase heat transfer components of heat flux for all flow rates are similar, suggesting that the data in Fig. 5(a) for the total heat flux represents a superposition of single-phase and two-phase heat transfer components over the entire temperature range. We leverage this finding to develop a physics-based

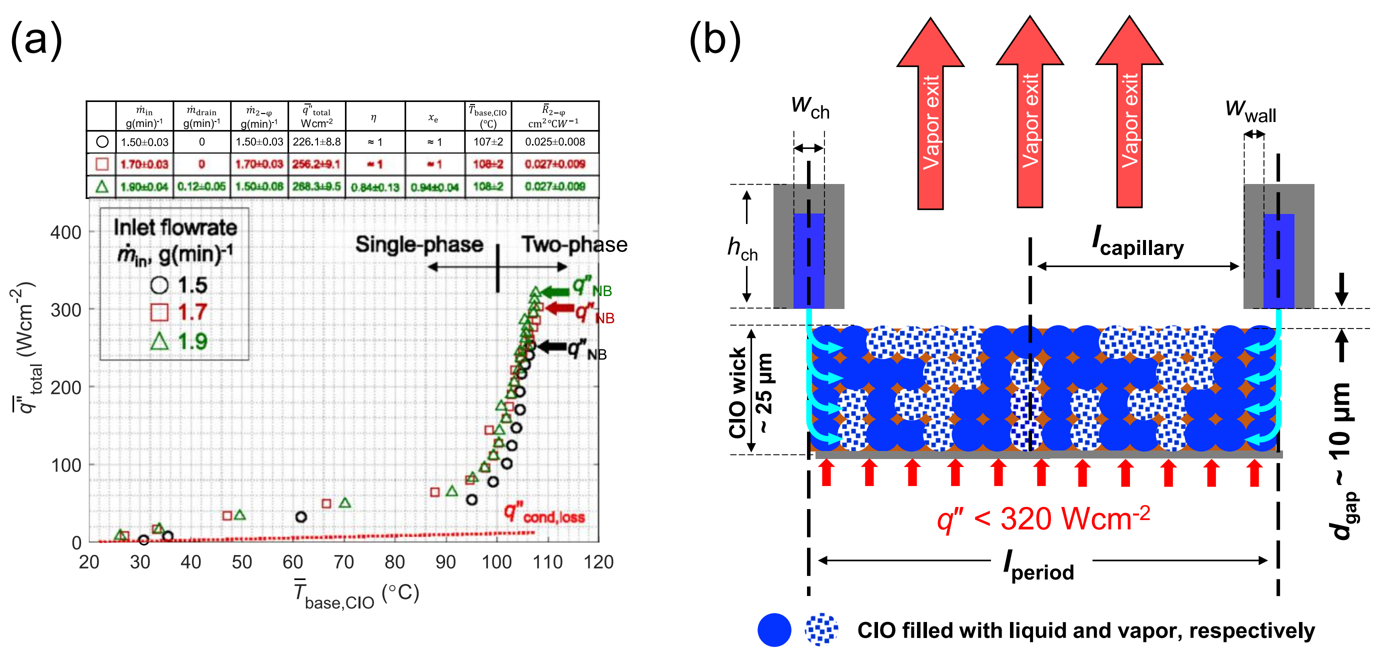

Fig. 4. Operation of the capillary-based micro-cooler in a two-phase boiling regime. (a) For the low flow rates of 1.5, 1.7 and 1.9 g(min)$^{-1}$, boiling curves are plotted as a function of the mean base temperature of the CIO wick. Note that a vapor exit quality $x_e \approx 1$ indicates the best performance (low thermal resistance and superheat). Measured heat losses due to heat conduction are also plotted for reference. (b) A cross-section schematic of a micro-cooler where the exact amount of coolant is delivered and vaporized without excess liquid drainage. Under these conditions, the capillary pressure of the CIO is enough to overcome the liquid pressure drop in the silicon microchannel, allowing a mixture of liquid and vapor within the CIO. Note that the liquid channels are not bonded to the CIO, creating a liquid meniscus bridge across the ≈ 10 μm gap.

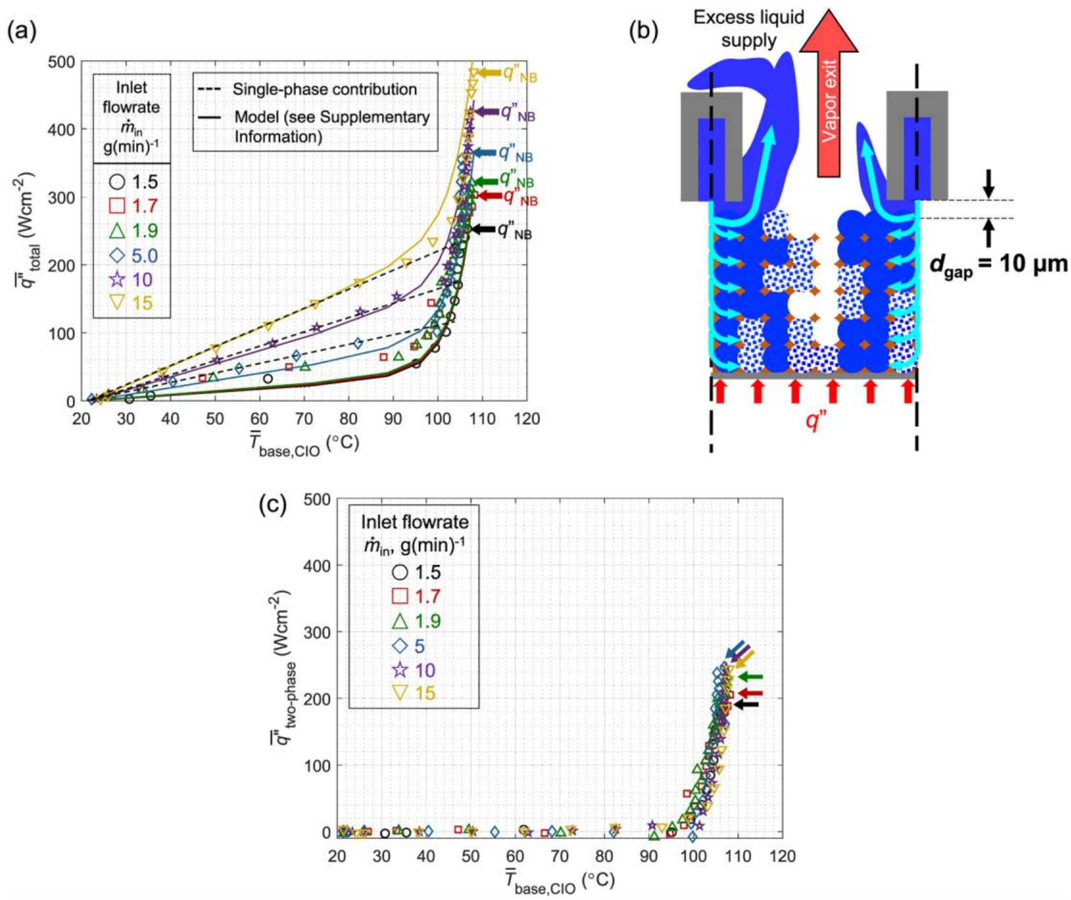

Fig. 5. (a) Boiling data (represented by markers) at different inlet flow rates of 1.5, 1.7, 1.9, 5, 10, and 15 g(min)$^{-1}$. The total heat flux applied to the heater is plotted as a function of the average base temperature of the CIO derived from the IR image over the heater using Eq. (2). For each flow rate, the corresponding modeling prediction curve is plotted in solid curves with the same color. For detailed information on the modeling, see Supplementary Information. The black dashed lines represent the contribution of single-phase heat transfer, as well as a small contribution from heat conduction loss. (b) The cross-sectional schematic of a micro-cooler with flow rates >1.9 g(min)$^{-1}$, where plenty of excess fluid is sloshing around due to vapor pressure, and then is drawn into the drainages (see Fig. 3). Residual liquid results in a "shallow" pool boiling condition that is expected to slightly increase superheat. (c) In this plot, we subtract the contribution of single-phase heat transfer, corresponding to black dashed lines in (a), from each data set for a given flow rate. Clearly, all the data collapse, indicating that the two-phase boiling contribution nearly remains the same, regardless of the flow rate.

model for the operation of the micro-cooler, which consists of convective single-phase and capillary-fed boiling heat transfer components as shown by the solid curves in Fig. 5(a). The modeling is further detailed in Ref. [36], and summarized in the Supplementary Information. The modeling results agree well with the data depicted in Fig. 5(a).

Table 3 provides additional information on the contribution of single-phase and two-phase heat transfer rates, as well as the exit vapor quality for any given flow rates just prior to the CHF. For the flow rates <1.9 g(min)$^{-1}$, the two-phase heat transfer effectiveness and the exit vapor quality are ≈ 1, because a negligible flow rate is measured at the drain. This highlights the best overall thermal performance and operational scenario for the micro-cooler, where achieving high two-phase heat transfer effectiveness and exit vapor quality represents the best use of the capabilities of the capillary-based micro-cooler. For higher flow rates, $\overline{q''}_{total,NB}$ increases, while the two-phase heat transfer effectiveness sharply decreases as the contribution of the single-phase cooling increases. This is attributed to the fact that the contribution from two-phase heat transfer remains nearly constant. The overall thermal resistance of the micro-cooler is dramatically reduced to 0.18 cm^2 °C W^{-1}, owing to the increased contribution by sensible heat transfer at higher flow rate.

Fig. 6 depicts the temperature profiles of the CIO wall for different inlet flow rates at the heat flux levels of $\overline{q''}_{total,NB}$ and $\overline{q''}_{CHF}$. The CIO wall temperature profiles are derived from the IR data over the 0.5 cm × 0.5 cm heater area by subtracting the temperature drop across the silicon substrate at each pixel. At the heat flux level of $\overline{q''}_{total,NB}$ (just below the

Table 3
Thermal performance at near CHF for different flow rates.

$\dot{m}_{in}$ g(min)$^{-1}$	$\dot{m}_{drain}$ g(min)$^{-1}$	$\dot{m}_{2-\varphi}$ g(min)$^{-1}$	$\overline{q''}_{2-\varphi}$ W cm^{-2}	$\overline{q''}_{total}$ W cm^{-2}	η	x_e	$\bar{T}_{heater}$ °C	$\bar{T}_{base,CIO}$ °C	$\overline{R''}_{2-\varphi}$ cm^2°CW^{-1}	$\overline{R''}_{overall}$ cm^2°CW^{-1}
1.50 ± 0.03	0	1.50 ± 0.06	226.1 ± 8.8	253.4 ± 0.3	≈ 1	≈ 1	116 ± 2	107 ± 2	0.025 ± 0.008	0.34 ± 0.01
1.70 ± 0.03	0	1.70 ± 0.06	256.2 ± 9.1	302.4 ± 0.3	≈ 1	≈ 1	119 ± 2	108 ± 2	0.027 ± 0.009	0.29 ± 0.01
1.90 ± 0.04	0.12 ± 0.05	1.50 ± 0.06	268.3 ± 9.5	320.2 ± 0.3	0.84 ± 0.13	0.94 ± 0.04	119 ± 2	108 ± 2	0.027 ± 0.009	0.27 ± 0.01
5.00 ± 0.10	3.27 ± 0.05	1.73 ± 0.11	260.7 ± 16.8	365.2 ± 0.4	0.33 ± 0.05	–	119 ± 2	106 ± 2	0.019 ± 0.007	0.23 ± 0.01
10.00 ± 0.20	8.12 ± 0.05	1.88 ± 0.21	283.3 ± 31.1	425.7 ± 0.4	0.17 ± 0.03	–	123 ± 2	107 ± 2	0.022 ± 0.007	0.20 ± 0.01
15.00 ± 0.30	13.08 ± 0.05	1.92 ± 0.30	289.3 ± 45.8	484.6 ± 0.5	0.11 ± 0.02	–	126 ± 2	108 ± 2	0.024 ± 0.007	0.18 ± 0.01

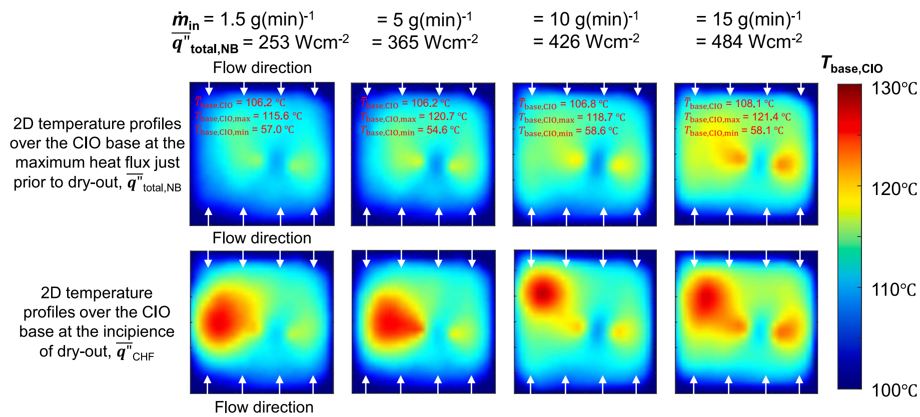

Fig. 6. 2D temperature profiles of the base (CIO side) that is derived from the measured IR images of the heater using Eq. (2). The profiles are presented at the maximum heat flux just before dry-out and at the heat flux where local hot spots begin to form, for different inlet flow rates used in the experiment. Note that the 2D temperature profiles of two-phase boiling are very similar, regardless of the flow rates, further confirming the results depicted in Fig. 5(c).

CHF), as the inlet flow rate is increased from 1.5 g(min)$^{-1}$ to 15 g (min)$^{-1}$, no significant increase in temperature is observed, despite the approximately two-fold increase in the total heat flux. This suggests that capillary-fed boiling is happening over the entire area of the CIO layer, which is not significantly impacted by the flow rate. In terms of the temperature distribution, the following features are noted: (a) the colder regions at the top and bottom of the image correspond to the availability of excess cold inlet liquid near the inlet plenums, (b) two (relatively) symmetric hot spot regions appear on the center-left and center-right of the chip. These could be attributed to variations in the gap spacing between the CIO wick and the silicon microchannels ($d_{gap} \approx 10$ μm), as depicted in Fig. 4(b) and 5(b), which could result in non-uniform supply of water due to a complex balance of capillary-fed liquid within the CIO wick and the microchannels. It is noted that the 3D manifold is secured but not directly bonded onto the CIO wick, which provides a great advantage in terms of the mechanical reliability of the micro-cooler. The temperature profiles in the second row show the representative snapshots of the local hot-spots (dark red color) just before the dry-out condition happens. These hot spots propagate rapidly across the heated area before the power supply is automatically turned off. The 2D temperature profiles at the stages of complete dry-out are presented in Fig. S1 in the Supplementary Information.

To gain further insight into the two-phase capillary-fed boiling and dry-out process, as well as flow patterns and bubble dynamics, we use the high-speed camera to capture a series of snapshot images at different flow rates and heat flux levels, as shown in Fig. 7. We present images at various CIO temperature levels: (1) prior to saturation temperature, (2) after saturation temperature, (3) half-way between saturation and dry-out temperatures, and (4) at the dry-out temperature. For each flow rate tested, ranging from 1.5 g(min)$^{-1}$ to 15 g(min)$^{-1}$, the data does not exhibit significant boiling prior to reaching the saturation temperature, which corresponds to the first column of images in the figure. Nevertheless, the incipience of bubble formation is observed, which is due to the degassing of liquid water. Beyond the saturation temperature, particularly at lower flow rates ranging from 1.5 to 5 g(min)$^{-1}$, turbulent mixing of the supplied liquid becomes evident due to vigorous boiling. However, at higher flow rate ranging from 10 to 15 g(min)$^{-1}$, this turbulent mixing is absent. It is inferred that at elevated flow rates, the large momentum of the liquid flow is not significantly affected by the vapor at low heat flux. Furthermore, small bubbles escaping from the wick are observed through the liquid film, compared to the cases at the heat fluxes before and after the saturation temperature. For low inlet flow rates ranging from 1.5 to 5 g(min)$^{-1}$, and at higher heat flux levels up to the CHF (3rd and 4th columns of the image set in Fig. 7), no excess liquid is observed in the open channels, which confirms the exit vapor quality is nearly one, and capillary-fed boiling prevails within the wick.

For high flow rates ranging from 10 to 15 g(min)$^{-1}$, a large volume of vapor interacts with a large volume of excess liquid, resulting in the breakup and swift removal of the thick excess liquid film from the surface of the wick. We designate the term "shallow liquid film boiling" regime to represent a hybrid single/two-phase boiling with very small superheat ($<$ 10 °C), in contrast with the large bubble formation observed in typical pool boiling tests, which often lead to large superheat ($>$ 10 °C) [25,31]. We also captured snapshots of the near-dry-out phase where a complete liquid depletion in the CIO wick is observed for low flow rates. However, for high flow rates, there is plenty of subcooled liquid present even under dry-out conditions. The 2D temperature profiles corresponding to the high-speed camera snapshot images in Fig. 7 are depicted in Fig. S3.

To better understand the underlying mechanisms of heat and mass transfer within the cooler, we present cross-sectional illustrations that qualitatively show the liquid flow and boiling dynamics, as seen in Fig. 7 (b-d). The color code for each illustration corresponds to the flow and heat transfer regimes depicted in the high-speed camera images. At low heat flux level, just before the onset of nucleate boiling (ONB) and near saturation temperature, the single-phase liquid coolants approximately follow distinct flow paths depicted by yellow arrows, removing heat from the CIOs, and eventually being moved sideways into drainage areas in the sample holder. Previous studies on single-phase liquid micro-coolers utilizing microchannel manifolds have demonstrated that an increase in flow rate leads to reduced thermal resistance of convective heat transfer [30,37]. This observation is attributed to the high flow velocity over the CIO surface, which in turn reduces the thermal boundary layer thickness and improves the heat transfer coefficient. These are consistent with our experimental results that show an increase in heat flux from 78 W cm^{-2} to 235 W cm^{-2} in the first column of Fig. 7 (a). At small inlet flow rates in combination with high heat flux levels, most of the supplied liquid is vaporized within the wick, as illustrated in Fig. 7(c). The inlet liquid flow rate is balanced with the vaporization rate of water within the CIO wick (vapor quality ~1). This is visually verified by the high-speed camera snapshots in Fig. 7(a), color-coded in magenta. When the flow rate exceeds the wicking capacity of the CIO layer, an interesting heat and mass transfer scenario occurs where *a shallow liquid pool boiling* regime prevails, as depicted in Fig. 7(d). It is postulated that the excess liquid flow is ejected through the gap between the CIO and the microchannel, indicated by yellow-colored arrows. The resulting shallow pool is expected to negligibly affect nucleate boiling within the CIO. This has been visually verified through high-speed camera images that capture the shallow pools splashed by vapor. It should be noted that the vaporization rate of water remains consistent across varying flow rates, as detailed in Table 3. At heat flux levels near the CHF point, corresponding to the fourth column of the high-speed

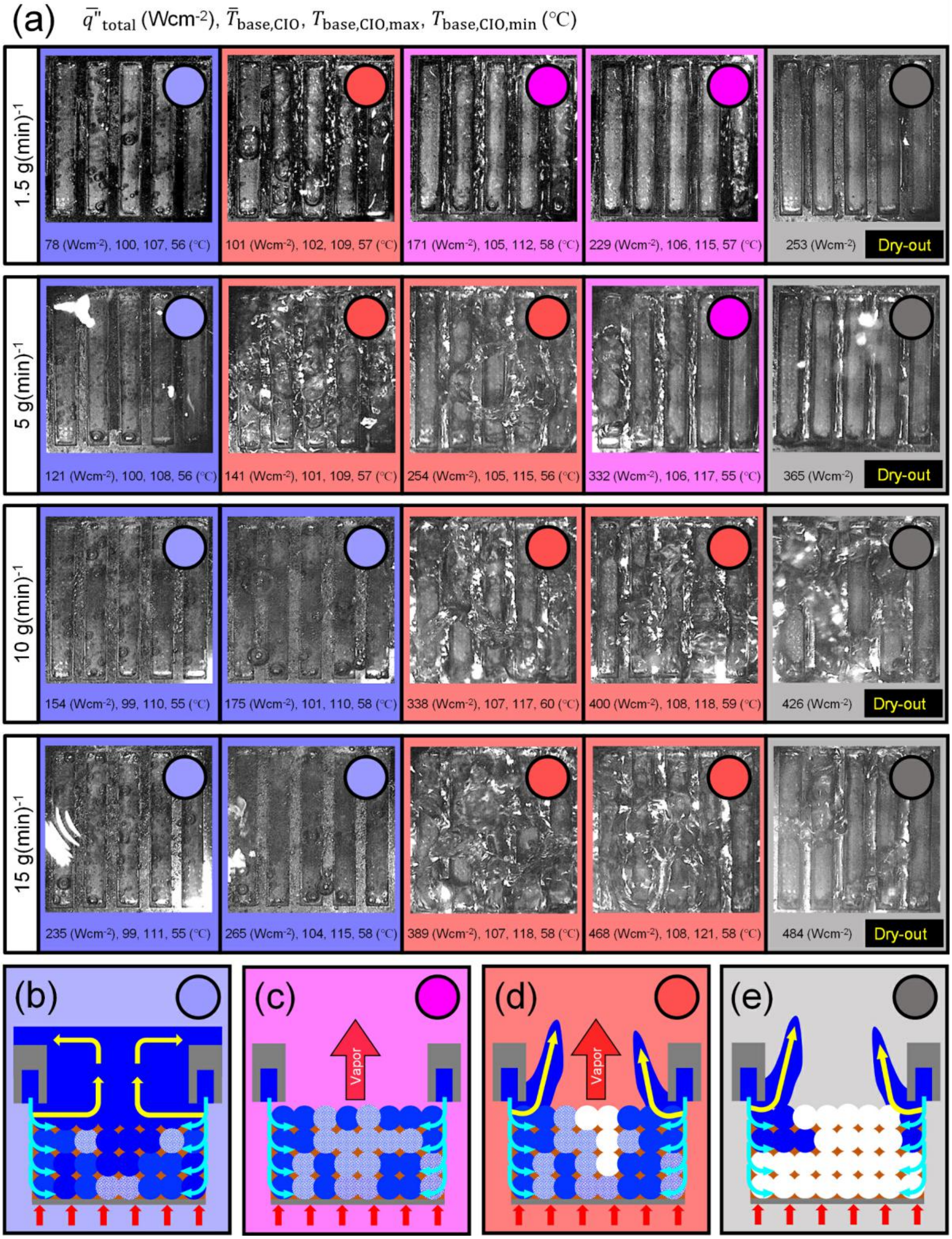

Fig. 7. (a) Representative snapshot images captured using high-speed camera for different heat fluxes and inlet flow rates. For each flow rate, the heat flux value is chosen ($\overline{T}_{\text{base,CIO}}$ = 99–100 °C) prior to and ($\overline{T}_{\text{base,CIO}}$ = 101–102 °C) after the water saturation temperature at the CIO base, in the middle of boiling ($\overline{T}_{\text{base,CIO}}$ = 105–107 °C), near $\overline{q}''_{\text{total,NB}}$, and finally during dry-out. The key hydrodynamic characteristics observed in the images are as follows: First column, there is no significant boiling; second column, turbulent mixing of liquid due to vigorous boiling at low flow rates, while, at higher flow rates, the turbulent mixing is absent and small bubbles escaping from the wick are observed through the liquid film; Third and Fourth columns, the negligible excess liquid exits out of the gap between the neighboring microchannels of the 3D manifold at low flow rates. At high flow rates, flow instability and shallow pool boiling prevails, while the CIO is not fully covered by the thick liquid film due to vapor escaping from the wick. Fifth column images show the liquid depletion over the entire heated area during the dry-out process. (b-e) Illustrations that show the scenarios of heat and mass transfer corresponding to the high-speed camera images in (a). The color codes - blue, magenta, red, and gray from (b) to (e) - correspond to single-phase heat transfer, capillary-fed boiling, boiling with a shallow pool, and dry-out, respectively. These color codes represent the heat and mass transfer scenarios observed in the speed-camera images, which are color-coded in the same way in (a). (For interpretation of the references to color in this figure legend, the reader is referred to the web version of this article.)

camera images in Fig. 7(a), this consistency also suggests that boiling within the CIO wick is independent of the inlet liquid flow rate and the total heat transfer rate is the sum of sensible and latent (boiling) heat transfers. Lastly, Fig. 7(e) describes the dry-out condition of the wick, where the large volume of vapor within the wick impedes the re-wetting process. This leads to a complete dry-out of the CIO wick. Such mechanisms have been confirmed by several previous studies [38–41]. Moreover, the high speed camera images in the last column in Fig. 7(a) capture clear indications of extensive dry areas. The IR images presented in Fig. S3 further depict the rapid spread of local hot spots.

7. Conclusions

In summary, a capillary-assisted two-phase microfluidic cooler is demonstrated by combining a 3D silicon microchannel manifold and a porous copper wick structure. We use microfabrication techniques to fabricate the silicon-based microchannel manifold and cold plate with the 0.5 cm × 0.5 cm integrated heater at the backside of the chip. The microporous CIO wick structure having the same area as the heater is fabricated on the cold plate chip. The thermal performance of our micro-cooler is experimentally characterized. To understand the operation mechanism of the micro-cooler, we performed a detailed analysis of heat and mass transfer and boiling dynamics by using high-resolution IR camera and high-speed camera imaging. The experimental results are corroborated by a novel finite element model, which captures the intricate heat and mass transfer involving phase change in porous media along with single-phase liquid flow.

The optimal overall (pumpless) performance was achieved at the low flow rate of 1.7 $g(min)^{-1}$, where the heat transfer coefficient ≈ 0.33 MW $m^{-2}\,{}^{\circ}C^{-1}$ (corresponding to $\overline{R''}_{2-\varphi} \approx 0.03$ $cm^2\,{}^{\circ}C\,W^{-1}$) was achieved at the two-phase component of total heat flux ≈ 250 W cm^{-2}, and the two-phase heat transfer effectiveness or vapor exit quality ≈ 1, signifying complete vaporization of water across the wick. In capillary-enhanced two-phase cooling systems, the “coolant” should be delivered as close as possible to its saturation temperature (100 °C for water), which allows for energy-efficient operations in data centers by reducing the energy needed to chill the coolant. A higher CHF reaching 485 W cm^{-2} is demonstrated by increasing the inlet mass flow rate to 15 $g(min)^{-1}$. This increase in CHF is attributed entirely to the additional contribution of single-phase heat transfer to the contribution of two-phase heat transfer, which decreases two-phase heat transfer effectiveness to ≈ 0.13.

The findings presented in this study are important for the reliable operation of high-heat-flux electronics with high cooling efficacy while minimizing associated costs for the electronics cooling. Furthermore, they offer key insights into the design and optimization of capillary-enhanced two-phase cooling technologies. Future research focuses on enhancing the boiling heat transfer coefficient by engineering the wick structure and by area scaling of the microcooler to 1 to 9 cm^2, without diminishing the overall cooling performance.

CRediT authorship contribution statement

Heungdong Kwon: Writing – review & editing, Data curation, Formal analysis, Methodology, Visualization, Writing – original draft. **Qianying Wu:** Writing – review & editing, Validation, Methodology, Formal analysis, Data curation. **Daeyoung Kong:** Writing – review & editing, Methodology, Data curation. **Sougata Hazra:** Methodology, Writing – review & editing. **Kaiying Jiang:** Formal analysis, Methodology, Writing – review & editing. **Sreekant Narumanchi:** Investigation, Writing – review & editing. **Hyoungsoon Lee:** Investigation, Writing – review & editing. **James W. Palko:** Investigation, Writing – review & editing. **Ercan M. Dede:** Investigation, Writing – review & editing. **Mehdi Asheghi:** Conceptualization, Project administration, Writing – original draft, Writing – review & editing. **Kenneth E. Goodson:** Conceptualization, Funding acquisition, Investigation, Project administration, Supervision, Writing – review & editing.

Declaration of competing interest

The authors declare the following financial interests/personal relationships which may be considered as potential competing interests:

Kenneth E. Goodson reports financial support was provided by Advanced Research Projects Agency-Energy. If there are other authors, they declare that they have no known competing financial interests or personal relationships that could have appeared to influence the work reported in this paper.

Data availability

Data will be made available on request.

Acknowledgment

We acknowledge financial support from the Advanced Research Projects Agency-Energy (ARPA-E) under the agreement DE-AR0001055, “Exploring the limits of cooling for extreme heat flux applications: data centers and power electronics”). Part of this work was performed at the Stanford Nanofabrication Facility (SNF) and Stanford Nanofabrication Shared Facilities (SNSF), supported by the National Science Foundation under award ECCS-2026822.

This work was co-authored in part by the National Renewable Energy Laboratory (NREL), operated by Alliance for Sustainable Energy, LLC, for the U.S. Department of Energy (DOE) under Contract No. DE-AC36-08GO28308. Funding provided by ARPA-E. The views expressed in the article do not necessarily represent the views of the DOE or the U.S. Government. The U.S. Government retains and the publisher, by accepting the article for publication, acknowledges that the U.S. Government retains a nonexclusive, paid-up, irrevocable, worldwide license to publish or reproduce the published form of this work, or allow others to do so, for U.S. Government purposes.

Appendix A. Supplementary data

Supplementary data to this article can be found online at https://doi.org/10.1016/j.icheatmasstransfer.2024.107592.

References

[1] K. Ebrahimi, G.F. Jones, A.S. Fleischer, A review of data center cooling technology, operating conditions and the corresponding low-grade waste heat recovery opportunities, Renew. Sust. Energ. Rev. 31 (2014) 622–638.

[2] B.K. Bose, Global energy scenario and impact of power electronics in 21st century, IEEE Trans. Ind. Electron. 60 (7) (2013) 2638–2651.

[3] A. Bar-Cohen, J.J. Maurer, A. Sivananthan, Near-junction microfluidic cooling for wide bandgap devices, MRS Adv. 1 (2) (2016) 181–195.

[4] A. Bar-Cohen, Gen 3 “embedded” cooling: key enabler for energy efficient data centers, IEEE Trans. Compon. Packag. Manuf. Technol. 7 (8) (2017) 1206–1211.

[5] D.B. Tuckerman, R.F.W. Pease, High-performance heat sinking for VLSI, IEEE Electron Dev. Lett. 2 (5) (1981) 126–129.

[6] E.M. Dede, C. Zhang, Q. Wu, N. Seyedhassantehrani, M. Shattique, S. Roy, J. W. Palko, S. Narumanchi, B. Kekelia, S. Hazra, K.E. Goodson, R. Giglio, M. Asheghi, Techno-economic feasibility analysis of an extreme heat flux micro-cooler, iScience 26 (1) (2023) 105812.

[7] S.M. Sohel Murshed, C.A. Nieto de Castro, A critical review of traditional and emerging techniques and fluids for electronics cooling, Renew. Sust. Energ. Rev. 78 (2017) 821–833.

[8] I. Mudawar, Assessment of high-heat-flux thermal management schemes, IEEE Trans. Components. Packag. Technol. 24 (2) (2001) 122–141.

[9] L. Zhang, E.N. Wang, K.E. Goodson, T.W. Kenny, Phase change phenomena in silicon microchannels, Int. J. Heat Mass Transf. 48 (8) (2005) 1572–1582.

[10] K.P. Drummond, D. Back, M.D. Sinanis, D.B. Janes, D. Peroulis, J.A. Weibel, S. V. Garimella, Characterization of hierarchical manifold microchannel heat sink arrays under simultaneous background and hotspot heating conditions, Int. J. Heat Mass Transf. 126 (2018) 1289–1301.

[11] M.B. Bowers, I. Mudawar, High flux boiling in low flow rate, low pressure drop mini-channel and micro-channel heat sinks, Int. J. Heat Mass Transf. 37 (2) (1994) 321–332.

[12] S.N. Joshi, E.M. Dede, Two-phase jet impingement cooling for high heat flux wide band-gap devices using multi-scale porous surfaces, Appl. Therm. Eng. 110 (2017) 10–17.
[13] E.N. Wang, L. Zhang, L. Jiang, J.M. Koo, J.G. Maveety, E.A. Sanchez, K.E. Goodson, T.W. Kenny, Micromachined jets for liquid impingement cooling of VLSI chips, J. Microelectromech. Syst. 13 (5) (2004) 833–842.
[14] M. Visaria, I. Mudawar, Application of two-phase spray cooling for thermal management of electronic devices, IEEE Trans. Components. Packag. Technol. 32 (4) (2009) 784–793.
[15] T.L. Cox, S.C. Yao, Heat transfer of sprays of large water drops impacting on high temperature surfaces, J. Heat Transf. 121 (2) (1999) 446–450.
[16] J.H. Kim, S.M. You, S.U.S. Choi, Evaporative spray cooling of plain and microporous coated surfaces, Int. J. Heat Mass Transf. 47 (14–16) (2004) 3307–3315.
[17] K.P. Drummond, D. Back, M.D. Sinanis, D.B. Janes, D. Peroulis, J.A. Weibel, S. V. Garimella, A hierarchical manifold microchannel heat sink array for high-heat-flux two-phase cooling of electronics, Int. J. Heat Mass Transf. 117 (2018) 319–330.
[18] J.A. Weibel, S.V. Garimella, M.T. North, Characterization of evaporation and boiling from sintered powder wicks fed by capillary action, Int. J. Heat Mass Transf. 53 (19–20) (2010) 4204–4215.
[19] R. Ranjan, S.V. Garimella, J.Y. Murthy, K. Yazawa, Assessment of nanostructured capillary wicks for passive two-phase heat transport, Nanoscale Microscale Thermophys. Eng. 15 (3) (2011) 179–194.
[20] M.S. El-Genk, A.F. Ali, Enhancement of saturation boiling of PF-5060 on microporous copper dendrite surfaces, J. Heat Transf. 132 (7) (2010).
[21] F. Zhou, J. Zhou, X. Li, Q. Chen, X. Huai, Enhanced capillary-driven thin film boiling on cost-effective gradient wire meshes for high-heat-flux applications, Exp. Thermal Fluid Sci. 149 (2023).
[22] C. Li, G.P. Peterson, Y. Wang, Evaporation/boiling in thin capillary wicks (l)—wick thickness effects, J. Heat Transf. 128 (12) (2006) 1312–1319.
[23] D. Ćoso, V. Srinivasan, M.-C. Lu, J.-Y. Chang, A. Majumdar, Enhanced heat transfer in biporous wicks in the thin liquid film evaporation and boiling regimes, J. Heat Transf. 134 (10) (2012).
[24] J.W. Palko, C. Zhang, J.D. Wilbur, T.J. Dusseault, M. Asheghi, K.E. Goodson, J. G. Santiago, Approaching the limits of two-phase boiling heat transfer: high heat flux and low superheat, Appl. Phys. Lett. 107 (25) (2015).
[25] Q.N. Pham, S. Zhang, S. Hao, K. Montazeri, C.H. Lin, J. Lee, A. Mohraz, Y. Won, Boiling heat transfer with a well-ordered microporous architecture, ACS Appl. Mater. Interfaces 12 (16) (2020) 19174–19183.
[26] R. Chen, M.C. Lu, V. Srinivasan, Z. Wang, H.H. Cho, A. Majumdar, Nanowires for enhanced boiling heat transfer, Nano Lett. 9 (2) (2009) 548–553.
[27] C. Zhang, J.W. Palko, M.T. Barako, M. Asheghi, J.G. Santiago, K.E. Goodson, Enhanced capillary-fed boiling in copper inverse opals via template sintering, Adv. Funct. Mater. 28 (41) (2018).
[28] G.S. Hwang, E. Fleming, B. Carne, S. Sharratt, Y. Nam, P. Dussinger, Y.S. Ju, M. Kaviany, Multi-artery heat-pipe spreader: lateral liquid supply, Int. J. Heat Mass Transf. 54 (11−12) (2011) 2334–2340.
[29] Y. Nam, S. Sharratt, G. Cha, Y.S. Ju, Characterization and modeling of the heat transfer performance of nanostructured Cu micropost wicks, J. Heat Transf. 133 (10) (2011).
[30] K.W. Jung, C.R. Kharangate, H. Lee, J. Palko, F. Zhou, M. Asheghi, E.M. Dede, K. E. Goodson, Embedded cooling with 3D manifold for vehicle power electronics application: single-phase thermal-fluid performance, Int. J. Heat Mass Transf. 130 (2019) 1108–1119.
[31] H. Lee, T. Maitra, J. Palko, D. Kong, C. Zhang, M.T. Barako, Y. Won, M. Asheghi, K. E. Goodson, Enhanced heat transfer using microporous copper inverse opals, J. Electron. Packag. 140 (2) (2018).
[32] Q. Wang, R. Chen, Ultrahigh flux thin film boiling heat transfer through nanoporous membranes, Nano Lett. 18 (5) (2018) 3096–3103.
[33] M.S. El-Genk, A.F. Ali, Enhanced nucleate boiling on copper micro-porous surfaces, Int. J. Multiphase Flow 36 (10) (2010) 780–792.
[34] R.J. Moffat, Describing the uncertainties in experimental results, Exp. Thermal Fluid Sci. 1 (1) (1988) 3–17.
[35] C. Zhang, J.W. Palko, M.T. Barako, M. Asheghi, K.E. Goodson, Design and optimization of well-ordered microporous copper structure for high heat flux cooling applications, Int. J. Heat Mass Transf. 173 (2021).
[36] Q. Wu, Capillary-Driven Boiling and Adsorptive Water Harvesting: Enhancing Water and Energy Efficiency in Data Center Cooling, PhD thesis, Stanford University, Stanford, CA, 2024.
[37] R. van Erp, R. Soleimanzadeh, L. Nela, G. Kampitsis, E. Matioli, Co-designing electronics with microfluidics for more sustainable cooling, Nature 585 (7824) (2020) 211–216.
[38] T.G. Theofanous, T.N. Dinh, J.P. Tu, A.T. Dinh, The boiling crisis phenomenon, Exp. Thermal Fluid Sci. 26 (6–7) (2002) 793–810.
[39] S.J. Kim, I.C. Bang, J. Buongiorno, L.W. Hu, Surface wettability change during pool boiling of nanofluids and its effect on critical heat flux, Int. J. Heat Mass Transf. 50 (19–20) (2007) 4105–4116.
[40] T. Semenic, I. Catton, Experimental study of biporous wicks for high heat flux applications, Int. J. Heat Mass Transf. 52 (21−22) (2009) 5113–5121.
[41] E. Forrest, E. Williamson, J. Buongiorno, L.-W. Hu, M. Rubner, R. Cohen, Augmentation of nucleate boiling heat transfer and critical heat flux using nanoparticle thin-film coatings, Int. J. Heat Mass Transf. 53 (1–3) (2010) 58–67.